Rock Mech Rock Eng (2011) 44:415–430
DOI 10.1007/s00603-011-0156-3

ORIGINAL PAPER

Experimental Study of the Brittle Behavior of Clay shale in Rapid Unconfined Compression

Florian Amann · Edward Alan Button · Keith Frederick Evans · Valentin Samuel Gischig · Manfred Blümel

Received: 20 December 2010 / Accepted: 21 April 2011 / Published online: 6 May 2011

Abstract The mechanical behavior of clay shales is of great interest in many branches of geo-engineering, including nuclear waste disposal, underground excavations, and deep well drilling. Observations from test galleries (Mont Terri, Switzerland and Bure, France) in these materials have shown that the rock mass response near the excavation is associated with brittle failure processes combined with bedding parallel shearing. To investigate the brittle failure characteristics of the Opalinus Clay recovered from the Mont Terri Underground Research Laboratory, a series of 19 unconfined uniaxial compression tests were performed utilizing servo-controlled testing procedures. All specimens were tested at their natural water content with loading approximately normal to the bedding. Acoustic emission (AE) measurements were utilized to help quantify stress levels associated with crack initiation and propagation. The unconfined compression strength of the tested specimens averaged 6.9 MPa. The crack initiation threshold occurred at approximately 30% of the rupture stress based on analyzing both the acoustic emission measurements and the stress–strain behavior. The crack damage threshold showed large variability and occurred at approximately 70% of the rupture stress.

Keywords Unconfined compressive strength · Brittle failure · Anisotropic rock · Clay shale · Damage initiation · Acoustic emissions

F. Amann (✉) · K. F. Evans · V. S. Gischig
Engineering Geology, Institute of Geology,
Swiss Federal Institute of Technology,
Sonneggstrasse 5, 8092 Zurich, Switzerland
e-mail: florian.amann@erdw.ethz.ch

K. F. Evans
e-mail: keith.evans@erdw.ethz.ch

V. S. Gischig
e-mail: valentin.gischig@erdw.ethz.ch

E. A. Button
Geoconsult, Pvt. Ltd, Plot 473, Industrial Estate,
Udyog Vihar, Sector 19, Phase V, Gurgaon, India
e-mail: edward.button@geoconsult.eu

M. Blümel
Institute for Rock Mechanics and Tunnelling, Graz University of Technology, Rechbauerstrasse 12, 8010 Graz, Austria
e-mail: bluemel@tugraz.at

1 Introduction

The mechanical behavior of argrillitic rocks is of great interest in many branches of geo-engineering, including nuclear waste disposal, underground excavations and deep well drilling. Within these fields one of the most challenging problems facing engineers is assessing the stability of boreholes and underground excavations in increasingly higher stress regimes. With any underground cavity, the stress redistribution due to the excavation generates a considerable stress gradient where the near field conditions are dominated by very low confining stress. While many failure criteria utilized in engineering analysis are primarily based on the process of shear failure, observations in several argillaceous rock types consistently show that macroscopic extensional fracturing is involved in the failure process near the cavity (Blümling et al. 2007; Bossart et al. 2002; Martin et al. 2004; Corkum and Martin 2007; Rejeb and Cabrera 2006; Yong 2007; Millard et al. 2009). Thus, to correctly characterize and assess the near field behavior it is necessary to define the failure criteria with respect to the observed brittle failure process.

Studies investigating the failure behavior of brittle rock demonstrate that macroscopic tensile, rather than shear

failure modes, must be anticipated for a wide range of rock types when unconfined to slightly confined (Hoek and Bieniawski 1965; Hoek 1968; Cook 1965; Fairhurst and Cook 1966; Brace et al. 1966; Bieniawski 1967; Scholz 1968a, b; Tapponier and Brace 1976; Holzhausen and Johnson 1979; Feder 1980; Horii and Nemat-Nasser 1986; Martin 1997; Kaiser and Kim 2008a, b; Kaiser et al. 2010; Amann et al. 2010a). These studies suggest that nucleation, growth, and interaction of micro-cracks are the controlling processes that lead to macroscopic fracture and rupture of brittle solids under compression. Material heterogeneities or geometric discontinuities may produce local tensile stresses under far field compression, locally exceeding the tensile strength of the rock (Cook 1965; Scholz 1968a, b; Tapponier and Brace 1976; Horii and Nemat-Nasser 1986; Lan et al. 2010).

Laboratory studies and theoretical considerations on brittle rock behavior under unconfined compression revealed three key stress levels and four behavior stages (Fig. 1; Bieniawski 1967; Martin 1997).

At low axial load non-linear stress–axial strain behavior (behavior stage I) is often observed and can be attributed to closure of existing micro-cracks (Walsh and Brace 1966; Scholz 1968a, b). The micro-cracks are either pre-existing or induced during drilling, stress relaxation, specimen handling, specimen preparation or shrinkage.

The non-linear behavior is followed by linear elastic behavior (behavior stage II) and the stress–strain relationship is linear. As the axial stress increases, new micro-cracks may develop. The load where cracks start to grow is called the crack initiation stress (σ_{CI}) or damage initiation threshold (damage is defined as inelastic strain as a consequence of loading). It coincides approximately with the point where the stress–volumetric strain and stress–lateral strain curves depart from linearity (Brace et al. 1966; Bieniawski 1967; Lajtai and Lajtai 1974). This does not apply to the stress–axial strain curve that remains linear (Fig. 1). Brace et al. (1966) showed that for low-porosity rocks and concrete, the onset of cracking is initiated at 30–50% of the short-term uniaxial rupture stress. The stress threshold for micro-crack initiation has been confirmed in many studies on different rock types and is now widely accepted (Hallbauer et al. 1973; Scholz 1968a; Martin and Chandler 1994). Tapponier and Brace (1976) found that the extension of micro-cracks at σ_{CI} is mostly limited to the grain scale. Acoustic emission (AE) measurements have been shown to provide an accurate measurement of the crack initiation threshold (Scholz 1968a, b; Kranz and Scholz 1977; Lockner et al. 1992; Martin 1997). The crack initiation threshold is often regarded as the lower limit for both the in situ rock strength and the long-term strength if the rock is unconfined (Diederichs 2007).

Once the applied stress increases beyond the σ_{CI} threshold, damage accumulates in the specimen. Based on experimental studies and fracture mechanics principles Bieniawski (1967) postulated that two types of fracture propagation modes should be considered: stable and unstable fracture propagation (Fig. 1). Stable fracture propagation is generally a slow process, requiring an increase in stress (or strain) for each increment of crack growth. Unstable crack propagation cannot be controlled unless the stress is dropped. At the stress threshold related to unstable crack growth (σ_{CD}), the stress–axial strain curve typically deviates from linearity and the volumetric strain curve changes from contraction to extension. Volumetric strain reversal typically occurs between 0.7 and 0.9 of the rapid-loading rupture stress (Bieniawski 1967; Martin 1997). Macroscopic visible fractures are initiated at this level of axial stress, indicating strain localization associated with a critical crack density as a consequence of accumulated damage and crack coalescence (Lockner et al. 1992; Kemeny 1991; Hallbauer et al. 1973; Martin 1997). This threshold represents the upper limit of short-term in situ strength and is considered as the yield strength of the rock specimen (Bieniawski 1967; Diederichs et al. 2004).

The final stage of the failure process is rupture. Once the rupture stress (UCS) is reached, brittle solids show a

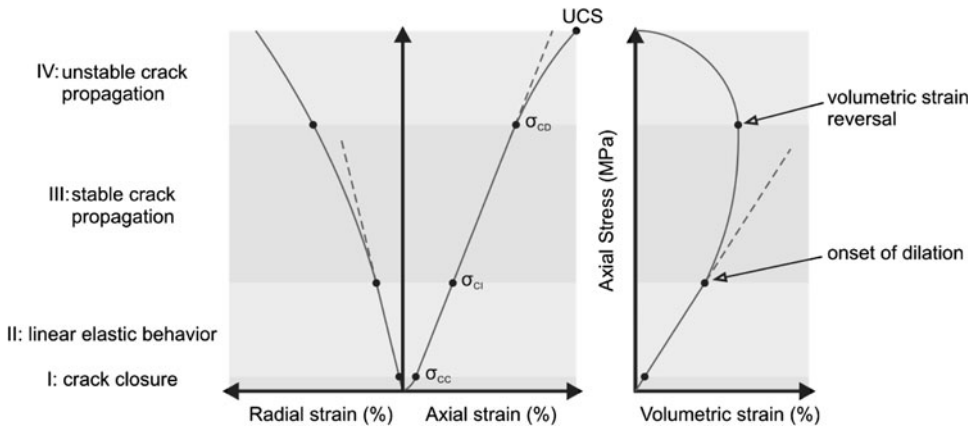

Fig. 1 Illustration of the critical stress thresholds and behavior stages for a brittle failing specimen under unconfined compressive loading

sudden strength drop associated with macro-scale fractures. The latter are typically aligned sub-parallel with the maximum principal stress leading to axial splitting.

Bieniawski (1967) pointed out that the modified Griffith failure criterion (Griffith 1921, 1924) constitutes a reliable indicator of crack initiation in brittle rocks. Since Griffith's fundamental work, many studies have shown that crack initiation in brittle rock is manifested as distributed Mode I fractures sub-parallel to the maximum compressive stress direction (e.g. Hoek and Bieniawski 1965; Hoek 1968; Cook 1965; Fairhurst and Cook 1966; Brace et al. 1966; Bieniawski 1967; Scholz 1968a, b; Lajtai 1974; Tapponier and Brace 1976; Lockner et al. 1992; Martin 1997). Tapponier and Brace (1976) investigated the micro-fracturing processes utilizing a scanning electron microscope (SEM) at individual loading stages of confined granite specimens (the confining stress was 50 MPa). They found that inelastic strains are almost entirely related to stress-induced crack initiation, growth, and propagation. Between the onset of dilation and the rupture stress, the crack density doubles and the increase of axial cracks is more than four times the increase in radial cracks.

The fundamental understanding of brittle failure behavior provides the bridge between fracture mechanics principles, empirical laboratory observations and near-excavation brittle rock mass behavior (Martin 1997; Kaiser et al. 2000; Diederichs 2003). The failure behavior around tunnels in moderately jointed, highly stressed brittle rock, is dominated by extensional Mode I fracturing (spalling). The development of such spalls can be related to stress-induced micro-crack initiation, crack growth and coalescence at the micro-scale (Horii and Nemat-Nasser 1985; Ewy and Cook 1990; Martin 1997; Kaiser et al. 2000; Germanovich and Dyskin 2000; Diederichs 2003; Lan et al. 2010) extending to the macro-scale. The observed macro-fractures are approximately aligned with the maximum principal stress which coincides with laboratory observations and theoretical expectations.

The experimental study presented here is motivated by the apparent brittle behavior of the argillaceous rock Opalinus Clay (OPA) observed during a number of mine-by studies in the Mont Terri Underground Research Laboratory (URL) (Bossart et al. 2002; Martin et al. 2004; Corkum and Martin 2007; Blümling et al. 2007; Yong et al. 2010). This relatively weak over-consolidated clay shale (Underwood 1967) has several advantageous characteristics for nuclear waste isolation, such as extremely low permeability and the potential for self-sealing, that make it the foremost candidate for selection as a host formation in Switzerland. However, the low strength, the strength anisotropy, and the observed brittle behavior (Bellwald 1990; Aristorenas 1992; Martin et al. 2004; Yong 2007; Blümling et al. 2007; Corkum and Martin 2007) are disadvantageous for the constructability of the disposal facilities. Observations made during a recent mine-by project (Thoeny et al. 2010) demonstrate that the bulk deformational behavior of OPA involves a combination of slip along bedding planes, slip along pre-existing fractures and brittle Mode I fracture processes (Amann et al., 2009, 2010b). Extensional macro-fractures were typically observed where only few pre-existing fractures were present.

A quantification of the stress thresholds where micro-cracks are initiated or propagate in an unstable manner is an important pre-requisite for designing repository structures. In the present study it is demonstrated that the failure behavior of unconfined OPA loaded normal to bedding is associated with brittle failure processes and σ_{CI} and σ_{CD} can be adequately determined by utilizing high-resolution strain measurements together with micro-acoustic emission monitoring. It is also shown that the strength and elastic anisotropy of the clay shale have a major influence on the fracture process and hence on the stress–strain response and acoustic activity. As sign convention compressive stress and contraction are denoted as positive.

2 Related Studies on the Behavior of Clay shales

Aristorenas (1992) and Bellwald (1990) studied the undrained and drained response of OPA specimens loaded under pure shear compression. During undrained specimen compaction, positive excess pore pressure was measured. As compressive shearing progressed, the specimens developed a tendency to dilate, accompanied by a continuous decrease of excess pore pressure. At failure, excess pore pressure was typically negative. Aristorenas (1992) showed that the dilatant behavior of OPA is due to micro-crack initiation, growth and interaction long before rupture stress is reached. Popp and Salzer (2007) investigated the short-term damage evolution of OPA specimens from the Mont Terri URL by performing true triaxial compression tests (confinement > 7.5 MPa). During the tests p- and s-wave velocity was continuously measured in both the axial and lateral direction. Based on velocity changes they inferred that inelastic deformation occurred at approximately 50–60% of the rupture stress. The inflection point of p-wave velocity changes was used to define the transition from net contraction to net dilation, and was approximately 80–90% of the peak strength. Naumann et al. (2007) showed that σ_{CD} was influenced by the bedding orientation from confined tests on OPA specimens (confining stress > 5 MPa) taken from the Mont Terri URL. For specimens loaded normal to bedding, σ_{CD} was on average 96% of the rupture stress. All the above studies utilized confined specimens and the failure mode was typically macroscopic shear failure. To the author's knowledge,

previous investigations to identify σ_{CI} and σ_{CD} for unconfined loading of OPA do not exist.

3 Material Description

The argillaceous rock OPA at the Mont Terri URL is a moderately over-consolidated claystone. Three main lithological facies have been identified at the URL: the shaly facies, the sandy facies and the carbonate-rich facies (Thury and Bossart 1999). Specimens utilized for this study were obtained from the shaly facies. According to Underwood (1967) the rock is classified as a clay shale.

The mass fractions of the predominant mineralogical components of the shaly facies are clay minerals (50–66%), quartz (10–20%), carbonates (8–20%) and feldspar (3–5%) (Thury and Bossart 1999; Klinkenberg et al. 2009). The mass fraction of clay minerals is composed of 20–30% 2:1 layer and mixed layer silicates, 7–8% chlorite and 20–25% Kaolinite (Klinkenberg et al. 2009). Clay platelets are tabular-shaped and lie sub-parallel with the macroscopic bedding, which is made up of siderite concretions and silt and sandstone lenses. Studies of the micro-fabric show that spatially distributed coarse grains in the OPA are mainly carbonate bioclasts (shell fragments) and pyrite (trace fossils) of different shapes and size (up to 1 mm), orientated typically sub-parallel to the bedding (Klinkenberg et al. 2009). The pronounced micro-fabric of the clayey matrix was formed by a complex history of sedimentation, burial, physical compaction, development of diagenetic bonding, tectonic faulting, uplift and erosion (Marschall et al. 2005; Van Loon et al. 2004). The maximum burial depth at the level of the Mont Terri URL is estimated to be 1,000 m in the late-Tertiary; the present burial depth is 200–300 m (Thury and Bossart 1999).

The physical properties of the OPA exhibit strong anisotropy. This is illustrated by the hydraulic conductivity obtained from laboratory and in situ experiments which is in the range of 0.6–0.7 $\times$ 10^{-13} m/s perpendicular to bedding and 1.3–2.0 $\times$ 10^{-13} m/s parallel to bedding (Bock 2008). The porosity of OPA varies between 12 and 18%. Mercury porosimetry data suggest that a large portion of the pores consists of equivalent pore radii in the micro- (equivalent radius < 25 nm) and macro-scale (equivalent radius > 25 nm). The fraction of macro-pores is estimated to be about 10% (Marschall et al. 2005).

4 Methods

4.1 Sampling, Specimen Characterization and Specimen Handling

Two 89-mm diameter cores (BRC-3 and BRC-4) were drilled with compressed air cooling in the Mont Terri URL to obtain high-quality specimens of the shaly facies. Specimens taken from triple-tube core barrels were hermetically sealed in vacuum-evacuated foil. Several specimens were weighed immediately after removal and dried at 105°C to a constant weight following I.S.R.M. (1979) suggested methods to determine the water content of fresh cores. Cylindrical specimens were carefully prepared by dry cutting and polishing the end faces in a lathe. Depending on the original specimen length and texture, a height-to-diameter ratio of 1.6–2.0 was utilized. The remaining pieces of each core were used to determine the mass fraction of water, ω. The volumetric water content, θ, was calculated using the following expression

$$\theta = \frac{\omega \times \rho_s}{(1-\omega) \times \rho_w + \omega \times \rho_s} \quad (1)$$

where ρ_w is the density of pore water (1 g cm^{-3}) and ρ_s is the grain density of rock (2.7 $\pm$ 0.2 g cm^{-3} (Bock 2008). The total porosity, ϕ, was derived from the dry bulk density ($\rho_{bulk,dry}$) and grain densities using,

$$\phi = 1 - \frac{\rho_{bulk,dry}}{\rho_s} \quad (2)$$

The dry bulk density was estimated by the mass after drying and the volume measured prior to drying. The saturation degree (S_w) corresponds to the ratio of volumetric water content over the total porosity. Prior to testing, a petrophysical description of each specimen was obtained. The ultrasonic p-wave velocity was determined in both the axial and lateral directions. The mechanical tests were usually conducted about 30 min after removal of the hermetically sealed packing to minimize changes in state and potential damage due to water loss.

4.2 Testing Procedure

The uniaxial compressive loading axis was oriented 85° $\pm$ 5° to the bedding planes. The tests were performed at the Technical University of Graz (Austria) using a modified MTS 815 servo-hydraulic rock testing system with digital feedback control. All tests were executed with impervious end-plates. Sixteen tests were performed on unjacketed specimen and three on jacketed specimens (No. 214.45, 214.46, 214.47). The specimens were jacketed with a 0.5-mm thick DuPont FEP Fluorocarbon Film.

Axial and circumferential strain gages were mounted onto the specimen at half of the specimen height to eliminate the influence of end effects on the strain measurements. Two axial strain gages (Type MTS Model 632. 11F-90), each with a measurement base-length of 50 mm, were firmly attached on opposite sides of the specimens. Circumferential strain (ε_{circ}) was calculated from the displacement measured by a single gage (Type MTS Model

632.21) attached to a chain wrapped tightly around the specimen (Fig. 2b). Volumetric strain (ε_v) was calculated from the sum of the arithmetic mean of the two axial strains (ε_{axial}) and twice times the circumferential strain ($\varepsilon_{axial} + 2\varepsilon_{circ}$). The inelastic volumetric strain component ($\varepsilon_{v,inel}$), which is related to micro-cracking, was defined as the difference between the measured volumetric strain and the linear elastic component of the volumetric strain defined at low axial stress ($\varepsilon_{v,inel} = \varepsilon_{v,elast} - \varepsilon_v$). Before testing of the rock specimens the strain gages were calibrated with a MTS calibrator frame (MTS Model 650.03). In addition a low-carbon steel cylinder (50 mm in diameter and 100 mm in height) was tested unconfined utilizing three loading and unloading stages between 25 and 75 MPa axial loads. The three cycles yielded an estimate for Young's moduli of 211 GPa, and for Poisson's ratio of 0.23. The manufacturer of the steel cylinder gives a Young's modulus of 210 GPa, and a Poisson's ratio of 0.22–0.25. This indicates the calibration of the strain gages and loading cell is correct.

The failure of unconfined or slightly confined brittle solids is commonly associated with the development of axial cracks, and the circumferential displacement as a function of axial load tends to increase disproportional compared to the axial displacement curve. Thus, the most appropriate feedback signal for controlling the load throughout the failure of the specimen is the circumferential displacement rate. The circumferential displacement rate was utilized as the controlling feedback signal. The selected rate was 0.08 mm/min for most specimens, although 0.10 mm/min was used for three specimens and 0.15 mm/min for one specimen (Table 1).

Since the distribution of strains within the continuously failing specimen is not uniform, the measured strains are dependent on the location of the strain gages relative to the macroscopic failure zone. Therefore, the stiffness-compensated piston displacement signal is used to calculate the total axial strain in the post-failure region.

4.3 Micro-Seismic Signal Detection

An acoustic emission monitoring system with a 4-channel transient-recorder was used to identify AE signals related to the sudden growth of micro-cracks or slip along existing crack surfaces (Fig. 2a). Events were detected with four piezoelectric transducers affixed with adhesive to the specimen's surface during nine tests (Fig. 2b). The 11-mm diameter transducers were mounted on 2-mm thick brass holders whose bottom face was machined to the radius of curvature of the specimens to achieve contact over the entire area. Based on experience with weak argillaceous rock types, the transducer (GMuG AE-BLs-12) was designed to a have the main sensitivity in a frequency band between 10 and 300 kHz. Amplification was achieved in two stages. The first stage was a pre-amplifier (GMuG VV30) with a 30 dB gain. Before the signal enters the transient recorder, a second stage of amplification was applied with a 20 dB gain. Triggering of the transient recorder was controlled by a pre-defined signal amplitude threshold at each channel. Recordings were triggered for all channels when the signal amplitude of one channel exceeded the threshold level. The sampling rate was 2–5 MHz.

Electromagnetic disturbances occasionally triggered the acquisition system and typically appeared as coherent arrivals on two or more channels. Such noise was eliminated during post-processing utilizing a low pass Butterworth filter with a corner frequency of 200 kHz.

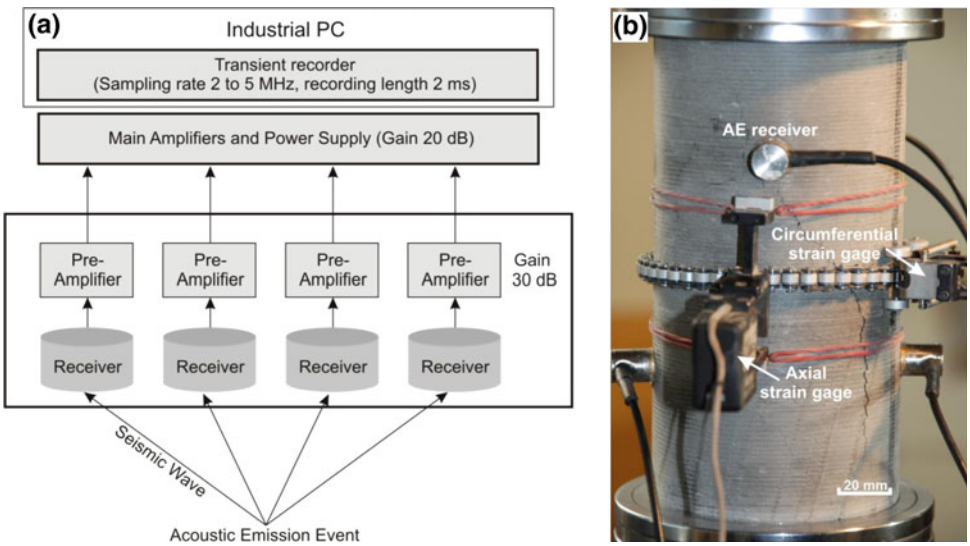

Fig. 2 **a** Schematic illustration of the experimental system for the detection of acoustic emissions (AE). **b** Experimental setup for uniaxial compressive strength tests with acoustic emission monitoring

Table 1 Circumferential displacement rate (CDR), volumetric water content (ω), p-wave velocity parallel ($V_{p,\parallel}$) and normal ($V_{p,\perp}$) to bedding, total porosity (Φ) and degree of saturation (S_w)

Specimen No.	CDR (mm/min)	ω (%)	$V_{p,\perp}$ (m/s)	$V_{p,\parallel}$ (m/s)	Φ	S_w
214.6	0.10	7.63	2,302	2,968	0.17	0.97
214.8	0.15	7.30	2,341	3,062	0.18	0.98
214.10	0.10	7.30	2,354	3,014	0.17	1.00
214.11	0.10	7.68	2,282	2,927	0.18	1.00
214.14	0.08	7.38	1,511	3,476	0.17	1.00
214.15	0.08	7.30	2,348	3,073	0.18	1.00
214.29	0.08	8.09	2,237	2,993	0.19	1.00
214.52	0.08	7.66	2,305	3,027	0.18	1.00
214.53	0.08	7.66	2,322	3,127	0.18	1.00
214.54	0.08	7.62	2,327	2,914	0.18	1.00
214.55	0.08	7.62	1,330	2,839	0.18	1.00
214.56	0.08	7.59	1,792	2,963	0.17	1.00
214.57	0.08	7.12	1,801	3,045	0.17	1.00
214.58	0.08	7.18	2,337	3,048	0.17	1.00
214.59	0.08	7.26	2,359	2,980	0.18	1.00
214.60	0.08	7.26	2,342	3,010	0.18	1.00
214.45[a]	0.08	7.88	2,253	3,061	0.18	1.00
214.46[a]	0.08	7.45	2,413	3,138	0.18	1.00
214.47[a]	0.08	7.81	1,749	2,742	0.18	1.00

All physical rock properties were determined before testing

[a] Jacketed specimens

4.4 Methodology for Defining Damage Stages

The crack initiation stress is usually determined by the point where the stress–volumetric strain curve departs from the linear elastic trend defined at lower stress levels (Brace et al. 1966). The Young's modulus and Poisson's ratio of a specimen were determined from the stress–strain curve by the least squares regression over the low stress range, where linear elastic behavior was evident (Fig. 1). The bulk modulus in this region was calculated according to the theory of linear elasticity. In terms of linear elasticity, the behavior of all specimens was never truly linear and a precise determination of the stress range defining elastic behavior was sometimes difficult (Fig. 1). In all cases, however, the first departure from linearity was clearly defined, and was taken as a lower limit of σ_{CI} (Fig. 3). In several tests, a distinct stress drop at low axial stress (approximately 2 MPa) occurred. Since the axial load for the test procedure is controlled by a constant circumferential displacement rate, this stress drop reflects a sudden increase of the lateral strain and indicates local failure. The stress level at which this stress drop occurred, if it occurred at all, was taken as the upper limit of σ_{CI} (Fig. 3). In all cases a mean value was calculated for σ_{CI}. This estimate of σ_{CI} coincides with the onset of continuous AE activity as also reported by Scholz (1968a, b); Kranz and Scholz (1977); Lockner et al. (1992); Martin (1997) and Eberhardt et al. (1998). Discontinuous AE activity (e.g. sporadic AE-events) at axial stress levels below σ_{CI} was only observed for specimen No. 215.54.

The stress level where unstable crack growth is initiated is usually taken as the reversal point of the stress–volumetric strain curve for unconfined compression tests (Bieniawski 1967; Diederichs and Martin 2010). As stated before, this behavior is dominated by a disproportional increase of lateral strain relative to the axial strain. For the material tested in this study, two types of volumetric behavior modes were observed: (1) the slope of the volumetric strain curve changes sharply at the reversal point and hence σ_{CD} can be reliably defined, and (2) the slope of the volumetric strain curve changes smoothly at the reversal point in which case the definition of a distinct value for σ_{CD} is difficult. To account for both cases, the upper and lower limits of σ_{CD} were taken as points on the volumetric strain curve where the volume strain differed by 0.002% from the maximum volumetric strain attained (Fig. 3). The axial stress at the reversal point of the volumetric strain curve was also determined.

5 Results

5.1 Specimen Characterization

Macroscopic inspection of the specimens revealed material heterogeneities in the form of silty or sandy nodules in specimen's No. 214.46 and 214.57, and some calcite veins in specimen 214.54.

The average mass fraction of water of the test specimens was 7.52% with a maximum of 8.09% and a minimum of 7.12% (Table 1). The fresh specimens attained a constant weight after 6–10 days of drying at 105°C. Figure 4 illustrates the water content measurements for both boreholes subsequent to drilling and after a period of storage, plotted against the vertical depth below the tunnel invert. Estimates obtained from fresh specimens immediately after removal from the borehole do not differ systematically from those made immediately after unwrapping following storage. The saturation was estimated as 1.0 for 16 specimens, and 0.97 and 0.98 for two specimens (Table 1).

The ultrasonic p-wave velocities measured after unwrapping are summarized in Table 1. The p-wave velocity parallel to the bedding plane ($v_{p,par} = 2{,}975 \pm 228$ m/s) was higher than perpendicular to bedding ($v_{p,perp} = 2{,}052 \pm 474$ m/s), and the mean anisotropy ratio ($v_{p,par}/v_{p,perp}$) was 1.45.

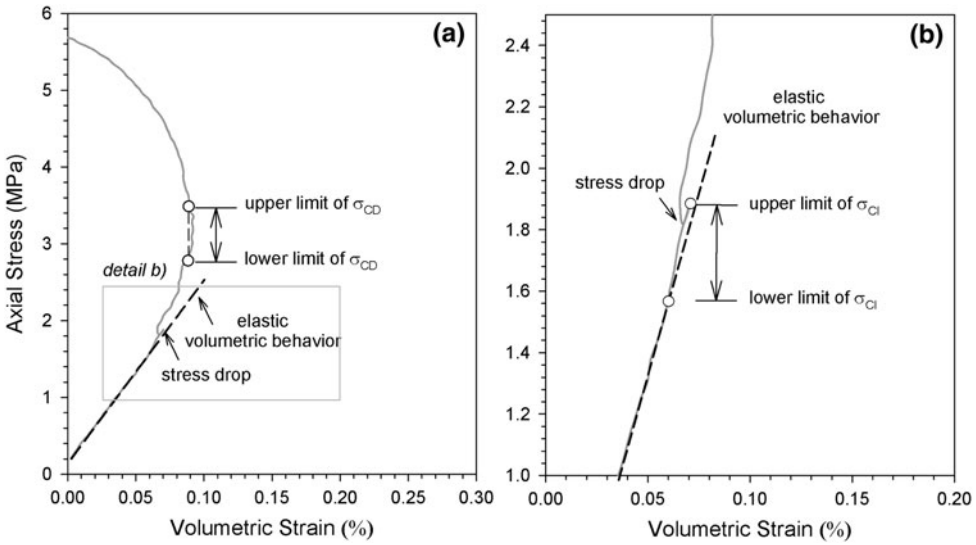

Fig. 3 Methodology for defining the upper and lower limit of damage stress thresholds (specimen No. 214.6). **a** Illustrates the deviation from linearity (onset of dilation σ_{CI} and the methodology for defining the crack damage threshold σ_{CD}). **b** expanded view of the *box* in **a** illustrating the procedure used to define the crack initiation threshold σ_{CI}

5.2 Stress–Strain Relationship

The stress–strain curves measured during the test on specimen 214.6 are shown in Fig. 5. They are typical for the curves of the most specimens. One exception was specimen No. 214.58, where the mean axial strain at axial loads less than 1 MPa showed slight non-linearity (e.g. a progressive increase in stiffness). Neither the ultrasonic velocity measurements nor the macroscopic characterization of this specimen revealed evidence of disturbance (Table 1). The minor non-linear anomaly is probably due to localized micro-cracks and/or compaction effects.

With increasing axial load, the stress–axial strain curve generally follow linear elastic behavior up to the onset of dilation at σ_{CI}. The elastic properties determined from the least squares best-fit to the linear portion of the stress–axial strain curve for each specimen are summarized in Table 2. On average, the elastic modulus for first loading was found to be 1.7 GPa with a minimum of 1.0 GPa and a maximum of 2.4 GPa. The Poisson's ratio ranged between 0.06 and 0.21 with a mean value of 0.16.

The onset of dilation occurred at an axial load of 1.5–2.5 MPa, the mean value being 2.0 MPa (Figs. 6, 7). This coincides for most specimens with a distinct stress drop which was taken as the upper limit for the onset of micro-cracking (Figs. 5, 6). Values of σ_{CI} taken from the stress–strain response revealed little scatter within experimental errors (Fig. 7). A distinct influence of the jacket on σ_{CI} was not apparent.

Figure 8 shows the crack initiation and crack damage thresholds in terms of the axial and circumferential strain. Both, the axial and circumferential strain at σ_{CI} show little

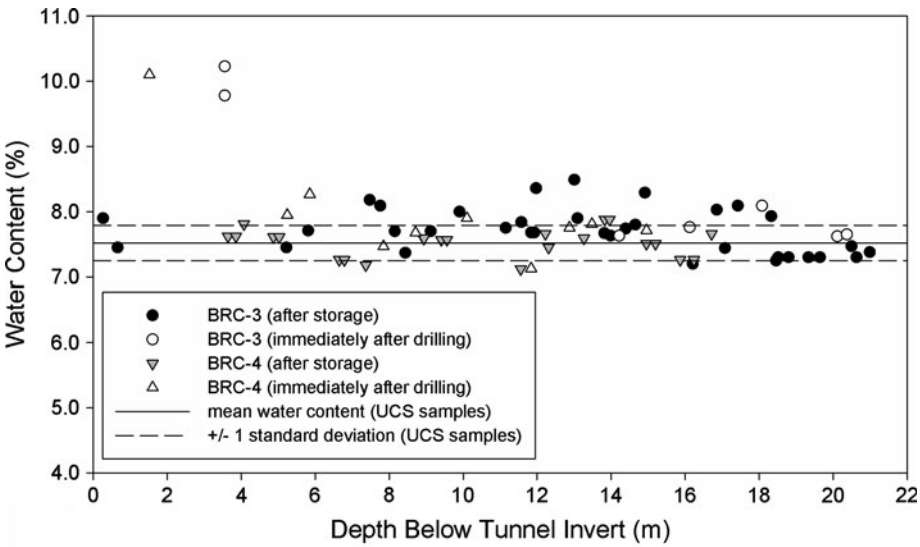

Fig. 4 Water content determined immediately after drilling and removal from storage versus depth below tunnel invert for both boreholes. No change in the water content during storage is evident

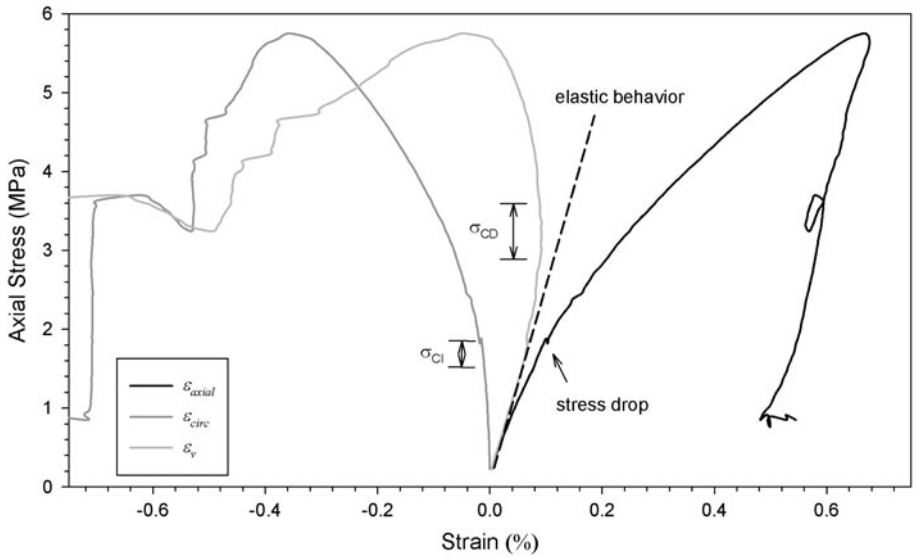

Fig. 5 Axial, circumferential and volumetric strain curves measured during the testing of specimen 214.6 under unconfined compressive load normal to bedding. The curves are typical of those obtained for most other specimens. The distinct stress drop at approximately 2.0 MPa was taken as a reliable indicator for micro-crack initiation. The *dashed line* represents the calculated elastic volumetric strain

Table 2 First loading Young's modulus (E), Poisson's ratio (υ), rupture stress (UCS), mean crack initiation stress taken from the stress–strain response (σ_{CI}), crack initiation stress taken from the acoustic emission signals ($\sigma_{CI,AE}$), point of volumetric strain reversal (σ_{CD})

Specimen No.	E (MPa)	υ	UCS (MPa)	σ_{CI} (MPa)	$\sigma_{CI,\ AE}$ (MPa)	σ_{CD} (MPa)
214.6	1,256	0.19	6.65	1.84	1.55	4.02
214.8	1,718	0.15	5.75	1.71	1.81	3.36
214.10	1,256	0.10	5.43	1.88	–	2.52
214.11	1,968	0.16	6.6	2.29	–	3.90
214.14	1,812	0.06	7.06	2.20	–	5.98
214.15	1,477	0.11	6.48	1.94	–	5.52
214.29	1,760	0.19	5.72	2.06	–	2.46
214.52	1,933	0.16	6.22	1.97	–	5.36
214.53	1,909	0.13	7.23	1.94	–	6.49
214.54	1,013	0.20	5.54	1.57	0.94	2.40
214.55	1,033	0.16	5.09	1.49	1.19	3.32
214.56	1,534	0.18	8.29	1.86	1.89	5.03
214.57	2,394	0.21	9.66	2.54	5.84	7.66
214.58	1,845	0.21	7.53	2.25	2.05	6.34
214.59	2,107	0.15	7.17	2.88	3.19	6.20
214.60	1,980	0.13	7.06	2.02	1.88	6.49
214.45[a]	2,134	0.16	8.70	2.14	–	4.62
214.46[a]	1,534	0.17	10.0	1.83	–	5.66
214.47[a]	1,423	0.21	5.63	1.87	–	4.57

Uncertainties of the damage stress thresholds are given in Fig. 7

[a] Jacketed specimens

variability. Crack initiation occurs at an axial strain of 0.07–0.16% and a circumferential strain of −0.01 to −0.04%.

Beyond σ_{CI} the strain curves increasingly depart from linearity (Fig. 5) with an associated increase in axial

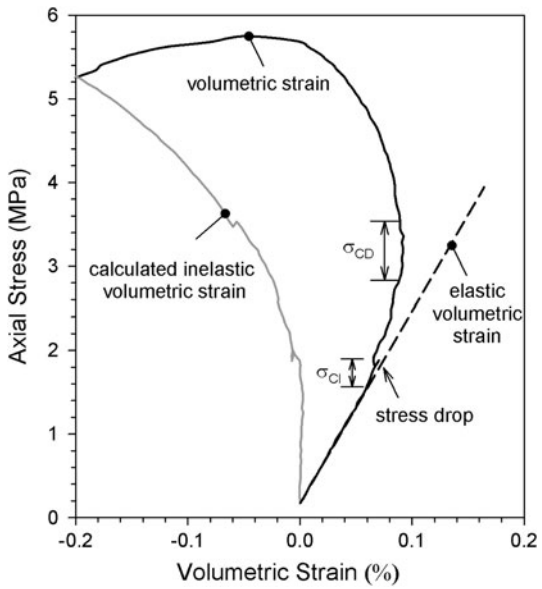

Fig. 6 Volumetric strain response and calculated elastic and inelastic volumetric strains obtained from the test of specimen No. 214.6. Inelastic strain is related to micro-cracking

compressibility and Poisson's ratio. The accelerating increase of inelastic volumetric strain results in a reversal of the volumetric strain curve (σ_{CD}), on average at 4.8 MPa (Table 2). The minimum value for σ_{CD} was 2.4 MPa, and the maximum value was 7.6 MPa (Fig. 7). Careful observation of the specimens during the tests revealed that σ_{CD} was associated with the appearance and opening of macroscopic fractures of 1–2 cm length sub-parallel with the loading direction (Fig. 9). The first observed fractures tended to cut at a high angle across bedding, while often stepping parallel to bedding on the millimeter scale. A distinct slope change of the axial and radial strain curve

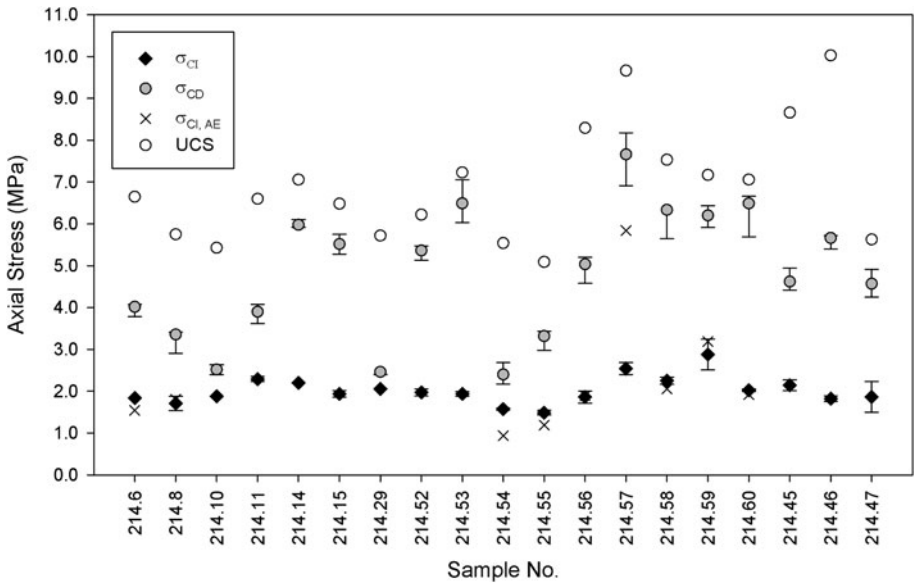

Fig. 7 Values of rupture stress (UCS), crack initiation threshold stress (σ_{CI}) and crack damage threshold stress (σ_{CD}) derived from the stress–strain curves and listed in Table 2. The estimates of σ_{CI} derived from the onset of continuous micro-acoustic activity are shown as *crosses* ($\sigma_{CI,\ AE}$). Specimens No. 214.45, 214.46 and 214.47 were jacketed

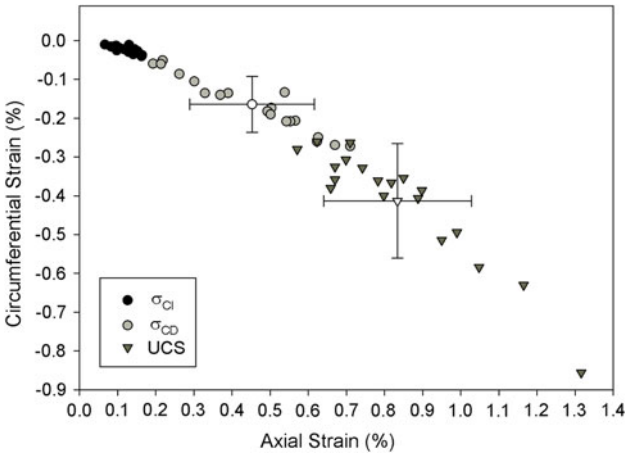

Fig. 8 Axial strain and circumferential strain at rupture stress (UCS), crack initiation (σ_{CI}) and crack damage (σ_{CD}) threshold. The variability of the axial and radial strain is illustrated for σ_{CD} and UCS with the mean and one standard deviation

at σ_{CD} was not observed. The values of σ_{CD} show larger variability than those of σ_{CI} (Fig. 7). The volumetric strain reversal obtained from all jacketed specimens (i.e. No. 214.45, 214.46 and 214.47) do not differ significantly to those for unjacketed specimens.

As the axial load was increased beyond σ_{CD}, the macroscopic fractures grew and were associated with increasingly more side-steps. The ultimate failure surface was typically 10°–20° inclined from the vertical specimen axis, primarily as a consequence of the side-steps (Fig. 9). This failure behavior was consistent for all tests.

Specimen rupture was characteristically accompanied by a sudden strength drop (Fig. 5). The unconfined compressive strength averaged over all specimens was 6.9 MPa. The highest UCS was 10.0 MPa, and the lowest 5.0 MPa (Fig. 7; Table 2). The highest UCS-values were found for specimens containing sandy or silty nodules (i.e. No. 214.46 and 214.57). On average the axial strain at rupture stress was 0.85%, and the circumferential strain was −0.43%, although the variability is very large (Fig. 8).

5.3 Micro-Acoustic Activity

For the nine tests with AE measurement, the maximum number of AE events triggered in the pre-rupture phase of any one specimen was 69, which is low compared to crystalline or hard sedimentary rock types (e.g. Scholz 1968b; Shah and Labuz 1995; Zang et al. 1996; Eberhardt et al. 1998; Diederichs et al. 2004; Heo et al. 2004; Baud et al. 2004).

Figure 10 illustrates the typical AE activity during a test. Almost no AE activity was observed at axial stress levels below 1.5–2 MPa, which is consistent with elastic behavior in this stress range. The onset of continuous AE, which was typically the start of the period of the highest AE-activity in the pre-rupture phase (Fig. 10), is in good agreement with σ_{CI} defined from the stress–strain response for seven out of nine specimens (Table 2; Fig. 7). The axial stress at the onset of continuous AE-activity for these seven specimens has an average value of 1.9 MPa, and was, on average, 29% of the rupture stress for each sample.

In the case of specimen No. 214.54, which contained calcite veins, the onset of AE activity appeared at an axial stress below σ_{CI} as defined from the stress–strain response, and was accompanied neither by a change in the curvature of the stress–strain curves nor a distinct stress drop. For specimen No. 214.57, which contained sandy nodules, the first AE signals were detected at stress levels significantly higher than σ_{CI} taken from the stress–strain response. The

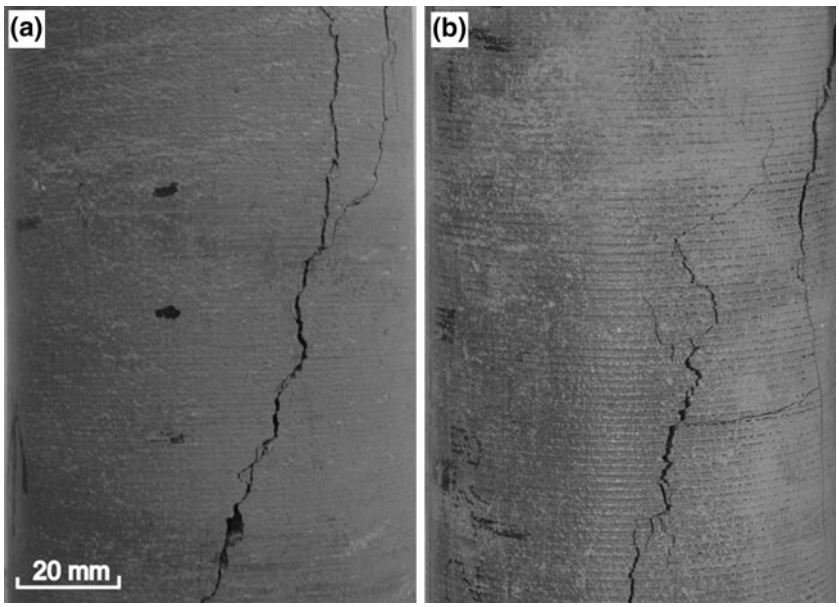

Fig. 9 Typical macroscopic failure of OPA specimens. In both figures a slightly inclined failure surface with well-developed side-steps can be seen

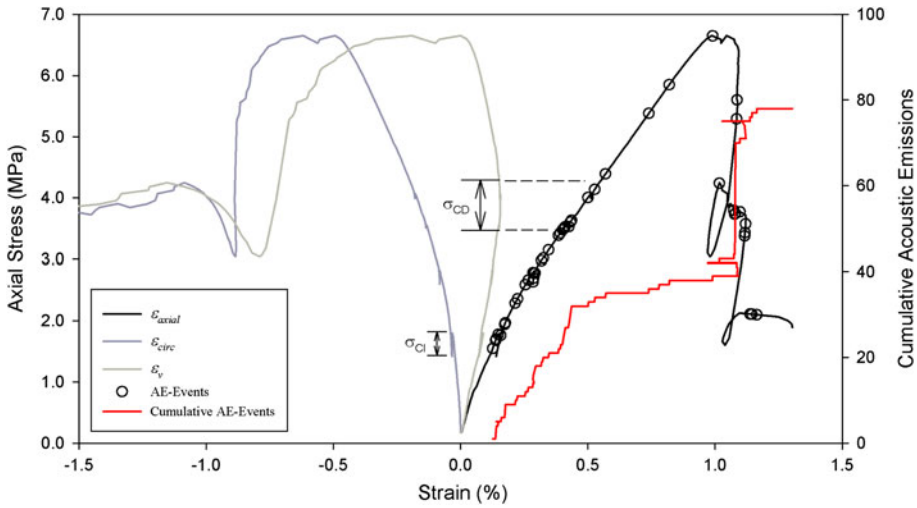

Fig. 10 Stress–strain response and acoustic emission activity for a typical OPA specimen (No. 214.6). *Circles* on the axial strain curve represent individual AE-signals. The crack initiation threshold σ_{CI} coincides well with the onset of continuous acoustic activity. The distinct reduction in acoustic activity corresponds to the crack damage threshold σ_{CD}

reasons for the difference between the AE onset and σ_{CI} for these two specimens are currently unclear.

With further stress increase beyond σ_{CI}, the overall AE-activity remained high, indicating a phase of intense micro-cracking activity. The majority of AEs were typically detected between σ_{CI} and σ_{CD}. This AE active phase was followed by a reduction in AE-signals (Fig. 10). For the majority of specimens, the reduction in AE-activity coincides with σ_{CD}.

When the axial stress approaches the rupture stress no change in the rate of acoustic emissions was observed. After the rupture stress was reached, an increase in acoustic emissions similar to the increase at σ_{CI} was typically recognized (Fig. 10).

6 Discussion

This experimental study on brittle failure of unconfined OPA revealed that the stress–strain response under short-term compression is linear elastic up to approximately 30% of the rupture stress. A first change in the stress–strain response appeared at a mean axial stress level of approximately 2 MPa and was associated with the onset of inelastic strain. This, together with the onset of AE-activity at approximately the same axial stress level, indicates that damage initiation occurs well before the rupture stress is reached, at least for these tests on OPA. However, the inferred ratio between crack initiation stress and rupture stress of approximately 0.3 is lower than observed in

confined compression tests (e.g. Popp and Salzer (2007) found a ratio of 0.4–0.5 for confining stresses larger than 7.5 MPa). The reasons for the difference are probably related to the failure mechanism, which changes from sub-vertical splitting when the specimens are unconfined to macroscopic shear failure when they are highly confined.

The data obtained in this study suggest that micro-crack initiation can be adequately identified from the stress–strain curves. However, for specimens equipped with AE-sensors, continuous AE-activity was initiated at a stress level slightly below σ_{CI}, although only by 0.1 MPa on average. The reason may be related to the strain monitoring system which only captures strains induced by micro-cracking within the base-length of the gages. Micro-cracks forming outside the base-length of the gages will not generate strain signals. Compaction effects perpendicular to the loading direction may also affect the determination of σ_{CI} as suggested by Popp and Salzer (2007). In either case, σ_{CI} obtained from OPA in this study has to be considered as an upper limit for damage initiation.

The presented data show little scatter for σ_{CI} (Fig. 6). Klinkenberg et al. (2009) studied failed OPA specimens taken from the shaly facies in the Mont Terri URL utilizing a scanning electron microscope. They found that cracks that grow either parallel or normal to bedding are often initiated at carbonate bioclasts (e.g. shell fragments) and are entirely situated within the clayey matrix. Fractures within bioclasts were not observed. Similar results were found for over-consolidated Callovo-Oxfordian argillites from the Bure site by utilizing SEM (Chiarelli 2000; Blümling et al. 2007) and other argillaceous rock under compressive loading (Fabre and Pellet 2006). These studies collectively suggest that macroscopic deformation is mainly due to cracking of the clayey matrix. Therefore, fracture initiation in OPA seems to be controlled by the strength of the apparently weaker clayey matrix. The small variability in σ_{CI} is possibly related to relatively homogeneous geomechanical properties of the weaker clayey matrix or individual bedding layers, where fractures are initiated.

As loading is increased beyond σ_{CI}, both, the radial and volumetric stress–strain curve deviate from linearity, as expected from theoretical considerations of unconfined compressive tests on brittle rock (Bieniawski 1967). However, Bieniawski (1967) also concluded that the axial stress–strain curve should remain linear for brittle solids under unconfined compression until the threshold stress for unstable crack growth σ_{CD} (coalescence of distributed micro-cracks) is reached. This is because the majority of distributed micro-cracks are true Mode I cracks that grow sub-parallel with the maximum far-field stress, and thus should not affect the axial strain as they form during the initial brittle damage phase (Bieniawski 1967). Many experimental and fracture mechanics studies on brittle material support Bieniawski's assertion (Brace and Bombolaski 1963; Scholz 1968a, b; Horii and Nemat-Nasser 1986; Martin 1997). However, the axial stress–axial strain curve for OPA does not show such behavior, but rather deviates from linearity above σ_{CI}, as do the radial and volumetric strain curves (Fig. 5). The axial compressibility thus begins to increase at σ_{CI} (Fig. 5). This indicates the activation of a fracture mode at σ_{CI} which affects the axial strain behavior.

A deviation of the stress–axial strain curve from linearity at stress levels below σ_{CD} (but above σ_{CI}) was reported by Eberhardt et al. (1998) for uniaxial loading tests on Lac du Bonnet Granite. They suggested that prior to the onset of unstable crack growth at σ_{CD}, coalescence of individual cracks occurred involving some micro-crack growth at oblique angles to the loading direction, accompanied by some shearing. The latter explains the deviation from linearity of the axial strain curve (Eberhardt et al. 1998). It should be noted that the deviation from linearity occurred at a load level distinctly higher than σ_{CI}, unlike the observations in the present study. Nevertheless, it suggests that perhaps the deviation of the stress–axial strain curve from linearity at σ_{CI} reflects the activation of shearing on oblique cracks as well as tensile opening of axial cracks.

Niandou et al. (1997) and Valès et al. (2004) conducted triaxial compression tests on anisotropic Tournemire Shale and found that the failure mode for unconfined or slightly confined compressive loading normal to bedding involved both, shear fractures that formed parallel to bedding and extensional fractures oriented normal to bedding. It is uncertain at what point in the failure process the bedding-plane shearing became active. Similar observations derive from examination of the pattern of the macroscopic fractures that are first seen on the walls of the OPA specimens at loads above σ_{CD} in the present study. The collective data do not define whether bedding-plane shearing begins internally at stress levels as low as σ_{CI}, and thus is a potential candidate to explain the change in axial stiffness at σ_{CI}. Thus, it is instructive to examine the conditions under which bedding-plane shearing can occur.

There is good reason to believe that the OPA specimens tested can be viewed as a laminate composed of bonded layers of different elastic properties oriented normal to the loading axis.

This is a consequence of its sedimentary origin. Bläsi (1996a, b) investigated heterogeneities on different scales in OPA utilizing thin-section analyses and SEM with an energy dispersive system. He showed that bed-to-bed material heterogeneities on the millimetre scale are present and reflect variations in the silt or sand content, bioclastic layers or siderite concretions. The lateral extension of these

layers or lenses is on the decimeter to meter scale (Bläsi 1996a, b; Nagra 2002). Such heterogeneities can be related to sedimentation in a deep basin (e.g. storm events) and diagenetic processes (Bläsi 1996a, b). Thus, the nature of the OPA leads to the view that the specimens are composed of a series of beds which have contrasting elastic parameters and strength on the millimeter to centimeter scale (Fig. 11a). Various theoretical and numerical models have been proposed to explain fracture formation and spacing in layered rock series (e.g. Price 1966; Hobbs 1967; Mandl 2005; Bai and Pollard 2000; Tang et al. 2008). Most studies consider a 3-layer model with a stiffer layer of some thickness sandwiched between more compliant layers. Bourne (2003) first derived an analytical solution in three dimensions for the stresses developed in an idealized layered system composed of bonded, planar, isotropic, homogeneous, linear elastic layers with contrasting elastic properties subjected to arbitrary layer-parallel and normal applied loads. The solution for the special case of uniaxial loading normal to layering under laterally unconfined conditions, as in the present experiments, shows that in-plane tension develops in the stiffer layers and corresponding compression in the more compliant layers (Fig. 11). (Note that these in-plane stress contrasts are accompanied by the development of a radial shear stress σ_{rz} on the interfaces). Axial tensile cracks will, thus, first initiate in the stiff layer when the radial tensile stress locally exceeds the tensile strength of the material (Fig. 11b). The axial load at this point is interpreted as denoting σ_{CI}. The axial growth of these tension cracks will tend to be arrested at the interface with the compressional compliant layers, possibly inducing local slip at the interface (Fig. 11b, Gudmundsson et al. 2003; Larsen and Gudmundsson 2010). Further axial loading of the layered system (which will increase the radial strain and thus increase the stress contrasts), will thus generate more tensile fractures in the stiff layers (infilling fractures). The generation of these cracks in relatively stiff layers can explain the observed increase in radial strain at σ_{CI}, but cannot by itself explain the change in axial compliance. We suggest two ways in which such a change might come about. The first is through the development of shear cracks in the compliant layers that link appropriately offset tensile cracks in the neighboring stiff layers (Fig. 11b). Such

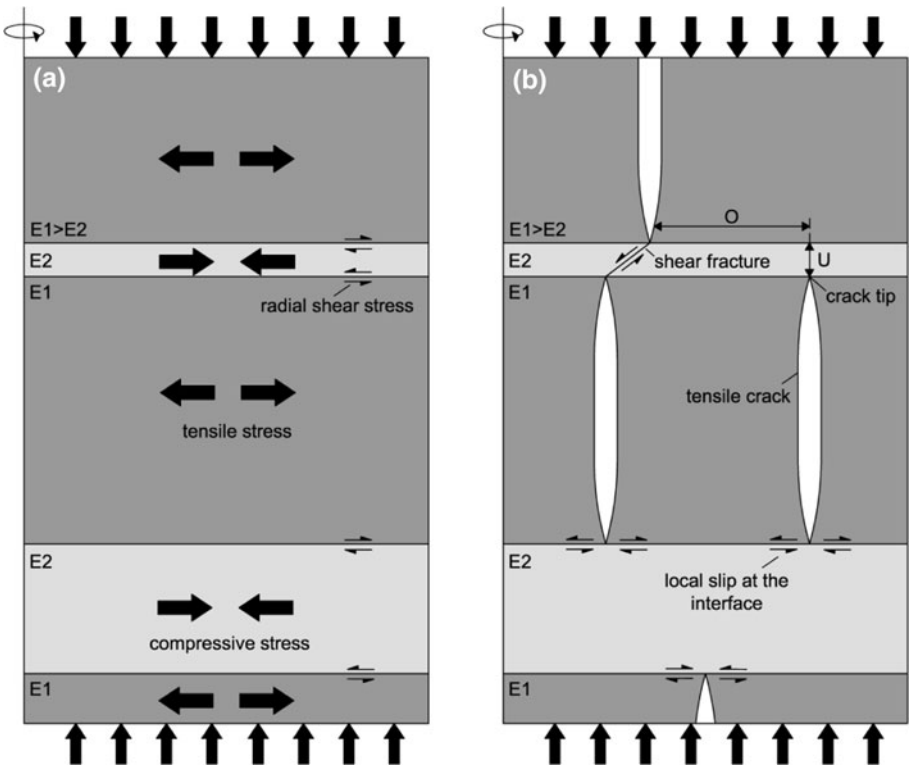

Fig. 11 Model for explaining crack initiation and the development of interfacial shear stress under uniaxial compressive load. The *left side* of the models represents the center line of a sample. **a** Model of the clay shale containing layers of contrasting stiffness (E1 > E2). In-plane tension develops in the stiffer layers and corresponding compression in the more compliant layers. These in-plane stress contrasts are accompanied by the development of a radial shear stress on the interfaces; **b** axial tensile cracks will thus first initiate in the stiff layer when the radial tensile stress locally exceeds the tensile strength of the material. The axial growth of these tension cracks will tend to be arrested at the interface with the compressional compliant layers, possibly inducing local slip at the interface. Appropriately offset tensile cracks in the neighboring stiff layers may be linked through the development of shear cracks in the compliant layer

tensile cracks would be underlapping (Gudmundsson et al. 2003). The second mechanism is poro-elastic in nature and involves the presence of fluid in the samples.

It is certain that pore space in the specimens is saturated, and thus the net compressive strain that develops up to σ_{CD} will result in an increase in pore pressure within the OPA matrix. The typical time for loading to reach the level of σ_{CI} in the experiments was 4 min, which is insufficient for the poro-elastically generated fluid pressure to dissipate. The precise pore pressure increase is difficult to estimate owing to the complex poro-elastic properties of the OPA (Aristorenas 1992), but some feeling for the anticipated values obtained by assuming that the conditions are fully undrained, and the rock is linear-elastic. In that case, the pore pressure at the time of fracture initiation would be, $P_p = B\sigma_{CI}/3$, where B is Skempton's coefficient. Taking B equal to 0.9 (Zhang et al. 2007) gives a pore pressures at σ_{CI} of approximately $P_p = 0.6$ MPa. Once the tensile cracks start to form in the stiffer beds when the axial load reaches σ_{CI}, fluid will be drawn into the cracks. The continual generation of these cracks as the axial load increases will drain fluid from the matrix resulting in the progressive depletion of pore pressure which would in turn affect the axial strain. The net effect would be to reduce the rate at which pore pressure increases under loading once axial cracks begin to form, and this could result in an increase in axial compliance.

A further observation that has not yet been addressed is the occurrence of a sudden drop in axial stress that occurs close to the level of σ_{CI} in 16 out of the 19 specimens tested. Since the axial load for the test procedure is controlled by a constant circumferential displacement rate, such a stress drop reflects a sudden increase of the lateral strain associated with local failure. Two speculative explanations for these events are proposed: (1) they reflect the simultaneous nucleation and propagation of micro-cracks, or (2) they reflect the propagation of pressurized cracks (hydrofractures) through the neighboring compliant layers.

Volumetric strain reversal (i.e. σ_{CD}) was approached in this study at approximately 70% of the rupture stress, which is in reasonable agreement with the findings of Popp and Salzer (2007) on confined OPA specimens (confinement > 7.5 MPa). The onset of net volumetric dilation associated with the first appearance of macroscopic fractures is consistent with observations made in previous studies on brittle rocks (Bieniawski 1967; Eberhardt et al. 1998; Martin 1997). Scholz (1968a) suggested that a critical crack density must be reached before regions do not fracture independently or, in other words, macro-fractures start to form. The formation of macro-fractures at σ_{CD} coincides for many rock types with a distinct rise in AE-activity (Mogi 1962; Scholz 1968b; Shah and Labuz 1995; Eberhardt et al. 1998; Diederichs et al. 2004; Heo et al. 2004). However, this does not seem to be the case for OPA. Actually, a distinct reduction in AE-activity occurred close to σ_{CD}. With further stress increase beyond σ_{CD} axial compressibility and Poisson's ratio increased continuously while the AE-activity remained low. In addition, the rupture stress could not be correlated to a particular acoustic emission sequence. This finding implies that beyond σ_{CD}, the damage process changes to a pre-dominant fracture mode with few or no local events involving rapid stress drop and hence hardly any radiation of acoustic signals, at least in the ultrasonic frequency range and trigger amplitude threshold utilized in this study.

With further specimen damage increasingly more side-steps appeared joining extensional fractures leading ultimately to the development of a failure surface approximately 10°–20° inclined from the vertical specimen axis.

The stress–strain response and the acoustic activity suggest that the failure process of OPA is associated with the formation of distributed micro-cracks (axial cracks and possibly shears) at loading levels between σ_{CI} and σ_{CD}. Micro-cracks are formed either in vicinity of heterogeneities such as shell fragment or probably in stiff layers when the radial tensile stress locally exceeds the tensile strength of the material (Fig. 11; Mandl 2005; Stefanizzi et al. 2008).

Observed hairline cracks at σ_{CD} associated with side-steps also suggest that shear stress is present along bedding planes. Beyond σ_{CD} increasingly more side-steps appear while the acoustic activity remains low. This implies that the damage process beyond σ_{CD} involves increasingly more fracture processes which hardly radiate any AE. Failure localizes due to side-steps forming links between individual axial cracks.

As stated previously, σ_{CD} shows a larger variability than σ_{CI}. Klinkenberg et al. (2009) postulate for OPA specimens with higher content of isolated, coarse bioclasts (e.g. shell fragments are closer to each other) that micro-fractures can interact more easily and the rupture stress is smaller compared to specimens with less shell fragments (in absence of shell fragments cracks end in the matrix). Micro-fractures may also interact more easily due to the distribution of bedding-parallel layers, the contrast in rock mechanical properties between the layers and the thickness of layers.

Therefore the variability in σ_{CD} in this study is possibly related to differences in the distribution of heterogeneities which controls to certain extent the probability of interaction and coalescence of micro-cracks. Appropriate micro-structural analyses to explore this hypothesis are ongoing.

7 Conclusions

The brittle failure characteristics of saturated Opalinus Clay (shaly facies) under unconfined uniaxial compression normal to bedding were studied. The failure process is initiated at a stress level far before rupture stress (approximately 30% of UCS) through the formation of axial micro-cracks and probably bedding parallel shears, accompanied by the onset of dilation and continuous micro-acoustic activity. The low scatter in the crack initiation threshold is possibly related to strain localization around heterogeneities (e.g. bioclasts) or radial tensile stresses in stiffer layers and almost homogeneous strength properties of the clayey matrix or individual layers, where fractures are initiated. Volumetric strain reversal occurred at approximately 70% of the rupture stress. The variability may be associated with the content and distribution of bioclasts and contrasting rock mechanical properties of bedding parallel layers in the clay shale, which controls, to certain extent, the growth and the probability of coalescence of micro-cracks in the specimen.

In contrast to expectations from theory on brittle failure, the axial strain curve deviates from linearity at the crack initiation stress threshold. The increase in axial compressibility is probably related to a simultaneous development of axial fractures and local shearing along bedding planes.

Between the crack initiation and crack damage threshold the acoustic activity remains high indicating fracture processes associated with sufficient local events involving rapid stress drops to radiate acoustic signals. When axial stress approaches the crack damage threshold, reduction in AE-activity was observed. The reduction in AE-activity is possibly related to a change in the pre-dominant fracture mode hardly radiating any acoustic signals (e.g. no or minor local events involving rapid stress drops). Observations suggest local side-stepping along bedding to be the pre-dominant mode of fracturing beyond the crack damage stress threshold forming links between cracks aligned subparallel with the axial stress. This failure process is leading ultimately to the development of a stepped failure surface approximately 10°–20° inclined from the specimen axis.

Acknowledgments This study was funded by the Swiss Federal Nuclear Safety Inspectorate (ENSI). The authors would like to thank Prof. Dr. Peter Kaiser and one unknown reviewer for the thorough review and useful suggestions.

References

Amann F, Button EA, Thoeny R, Loew S (2009) RC-experiment, rock mass characterisation. ENSI Erfahrungs- und Forschungsbericht 2009:177–185

Amann F, Kaiser PK, Steiner W (2010a) Triggering swelling potential of anhydrite clay rocks by brittle failure processes. In: Zhao J, Labiouse V, Dudt J-P, Mathier J-F (eds) Rock mechanics and environmental engineering. Paper presented at European Rock Mechanics Symposium 2010, Lausanne, Switzerland. Taylor & Francis Group, London, pp 339–342. ISBN 978-0-415-58654-2

Amann F, Button EA, Blümel M, Toeny R (2010b) Insight into the mechanical behaviour of Opalinus Clay. In: Zhao J, Labiouse V, Dudt J-P, Mathier J-F (eds) Rock mechanics and environmental engineering. Paper presented at European Rock Mechanics Symposium 2010, Lausanne, Switzerland. Taylor & Francis Group, London, pp 759–762, ISBN 978-0-415-58654-2

Aristorenas GV (1992) Time-depended behavior of tunnels excavated in shale. Ph.D-thesis, Department of Civil Engineering, Massachusetts Institute of Technology, Massachusetts, USA

Bai T, Pollard DD (2000) Fracture spacing in layered rocks: a new explanation based on the stress transition. J Struct Geol 22:43–57

Baud P, Klein E, Wong T-F (2004) Compaction localization in porous sandstones: spatial evolution of damage and acoustic emission activity. J Struct Geol 26:603–624

Bellwald P (1990) A contribution to the design of tunnels in argillaceous rock. Ph.D-Thesis, Department of Civil Engineering, Massachusetts Institute of Technology, Massachusetts, USA

Bieniawski ZT (1967) Mechanism of brittle failure of rock. Part I. Theory of fracture process. Int J Rock Mech Min Sci Geomech Abstr 4(4):395–406

Bläsi HR (1996a) Mont Terri Technical Note 96-08, thin section analyses. Mont Terri Project

Bläsi HR (1996b) Mont Terri Technical Note 96-09, detailed descriptions of drill cores. Mont Terri Project

Blümling P, Bernier F, Lebon P, Martin CD (2007) The excavation damaged zone in clay formations time-dependent behaviour and influence on performance assessment. Phys Chem Earth 32:588–599

Bock H (2008) RA experiment—updated review of the rock mechanics properties of the opalinus clay of the mont terri url based on laboratory and field testing, Mont Terri Technical Report 2008-04

Bossart P, Meier PM, Moeri A, Trick T, Mayor J-C (2002) Geological and hydraulic characterization of the excavation disturbed zone in the Opalinus Clay of the Mont Terri Rock Laboratory. Eng Geol 66:19–38

Bourne SJ (2003) Contrast of elastic properties between rock layers as a mechanism for the initiation and orientation of tensile failure under uniform remote compression. J Geophys Res 108(B8): 1–11

Brace WF, Bombolaski EG (1963) A note on brittle crack growth in compression. J Geophys Res 68(12):3709–3713

Brace WF, Paulding BR, Scholz C (1966) Dilatancy in fracture of crystalline rocks. J Geophys Res 71(16):3939–3953

Chiarelli AS (2000) Experimental investigation and constitutive modeling of coupled elastoplastic damage in hard claystones. Doctoral thesis, Laboratory of Mechanics, University of Lille, Lille, France (in French)

Ch-L Zhang, Rothfuchs T, Su K, Hoteit N (2007) Experimental study of the thermo-hydro-mechanical behaviour of indurated clays. Phys Chem Earth 32:957–965

Cook NGW (1965) The failure of rock. Int J Rock Mech Min Sci 2:389–403

Corkum AG, Martin CD (2007) Modelling a mine-by test at the Mont Terri rock laboratory, Switzerland. Int J Rock Mech Min Sci 44:846–859

Diederichs MS (2003) Rock fracture and collapse under low confinement conditions. Rock Mech Rock Eng 36(5):339–381

Diederichs MS (2007) The 2003 Canadian Geotechnical Colloquium. Mechanistic interpretation and practical application of damage

and spalling prediction criteria for deep tunnelling. Can Geotech J 44:1082–1116
Diederichs MS, Martin DC (2010) Measurement of spalling parameter from laboratory testing. In: Zhao J, Labiouse V, Dudt J-P, Mathier J-F (eds) Rock mechanics and environmental engineering. Paper presented at European Rock Mechanics Symposium 2010, Lausanne, Switzerland. Taylor & Francis Group, London, pp 323–326. ISBN 978-0-415-58654-2
Diederichs MS, Kaiser PK, Eberhardt E (2004) Damage initiation and propagation in hard rock during tunnelling and the influence of near-face stress rotation. Int J Rock Mech Min Sci 41:785–812
Eberhardt E, Stead D, Stimpson B, Read RS (1998) Identifying crack initiation and propagation thresholds in brittle rock. Can Geotech J 35:222–233
Ewy RT, Cook NGW (1990) Deformation and fracture around cylindrical openings in rock. II. Initiation, growth and interaction of fractures. Int J Rock Mech Min Sci Geomech Abstr 27(5):846–859
Fabre G, Pellet F (2006) Creep and time-dependent damage in argillaceous rocks. Int J Rock Mech Min Sci 43:950–960
Fairhurst C, Cook NGW (1966) The phenomenon of rock splitting parallel to the direction of maximum compression in the neighborhood of a surface. In: Proceedings of the 1st congress of the international society of rock mechanics, Lisbon, pp 687–692
Feder GF (1980) Rock mechanics aspects of the "New Austrian Tunneling Method" (NATM). Paper presented at the Arlberg-Seminar 1980, American Engineering Society, USA
Germanovich LN, Dyskin AV (2000) Fracture mechanism and instability of openings in compression. Int J Rock Mech Min Sci 37:263–284
Griffith AA (1921) The phenomena of rupture and flow in solids. Philos Trans Roy Soc London A 221:163–197
Griffith AA (1924) Theory of rupture. In: Bienzo CB, Burgers JM (eds) Proceedings of the first international congress for applied mechanics. Technische Boekhandel and Drukkerij, Delft, pp 55–63
Gudmundsson A, Gjesdal O, Brenner SL, Fjeldskaar I (2003) Effects of linking up of discontinuities on fracture growth and groundwater transport. Hydrogeology J 11:84–99
Hallbauer DK, Wagner H, Cook NGW (1973) Some observation concerning the microscopic and mechanical behaviour of quartzite specimens in stiff, triaxial compression tests. Int J Rock Mech Min Sci Geomech Abstr 10:713–726
Heo J-S, Ch-I Lee, Jeon S (2004) Measurement of acoustic emission and source location considering anisotropy of rock under triaxial compression. Key Eng Mater 270–273:1574–1579
Hobbs DW (1967) The formation of tension joints in sedimentary rocks: an explanation. Geol Mag 104:550–556
Hoek E (1968) Brittle failure of rock. In: Zienkiewicz (ed) Rock mechanics in engineering practice, pp 99–124
Hoek E, Bieniawski ZT (1965) Brittle rock fracture propagation in rock under compression. Int J Frac Mech 1(3):137–155
Holzhausen GR, Johnson AM (1979) Analyses of longitudinal splitting of uniaxially compressed rock cylinders. Int J Rock Mech Min Sci Geomech Abstr 16:163–177
Horii H, Nemat-Nasser S (1985) Compression-induced microcrack growth in brittle solids: axial splitting and shear failure. J Geophys Res 90:3105–3125
Horii H, Nemat-Nasser S (1986) Brittle failure in compression: splitting, faulting and brittle-ductile transition. Phil Trans R Soc Lond A 319:337–374
I.S.R.M. (1979) Suggested methods for determining water content, porosity, density, absorption and related properties and swelling and slake-durability index properties. Int J Rock Mech Min Sci Geomech Abstr 16(2):141–156
Kaiser PK, Kim BH (2008a) Rock mechanics advances of underground construction and mining. In: Paper presented at Korea rock mechanics, Seoul, Korea, pp 1–16
Kaiser PK, Kim BH (2008b) Rock mechanics challenges in underground construction and mining. In: Potvin Y, Carter J, Dyskin A, Jeffrey R (eds) Paper presented at 1st southern hemisphere international rock mechanics symposium, Australia, pp 23–38
Kaiser PK, Diederichs MS, Martin CD, Sharp J, Steiner W (2000) Underground works in hard rock tunneling and mining. In: Paper presented at GeoEng2000, Melbourne, Australia, pp 841–926
Kaiser PK, Amann F, Steiner W (2010) How highly stressed brittle rock failure impacts tunnel design. In: Zhao J, Labiouse V, Dudt J-P, Mathier J-F (eds) Rock Mechanics and Environmental Engineering. Paper presented at European rock mechanics symposium 2010, Lausanne, Switzerland. Taylor & Francis Group, London, pp 27–38. ISBN 978-0-415-58654-2
Kemeny JM (1991) A model for non-linear rock deformation under compression due to sub-critical crack growth. Int J Rock Mech Min Sci Geomech Abstr 28:459–467
Klinkenberg M, Kaufhold S, Dohrmann R, Siegesmund S (2009) Influence of carbonate micofabric on the failure strength of claystones. Eng Geol 107:42–54
Kranz RL, Scholz CH (1977) Critical dilatant volume of rocks at the onset of tertiary creep. J Geophys Res 82(30):4893–4898
Lajtai EZ (1974) Brittle fracture in compression. Int J Fract 10(4):525–536
Lajtai EZ, Lajtai VN (1974) The evolution of brittle fracture in rock. J Geol Soc 130:1–16
Lan H, Martin CD, Hu B (2010) Effects of heterogeneity of brittle rock on micromechanical extensile behavior during compression loading. J Geophys Res 115:1–14
Larsen B, Gudmundsson A (2010) Linking of fractures in layered rocks: implication for permeability. Tectonophysics 492:108–120
Lockner DA, Moore DE, Reches Z (1992) Microcrack interaction leading to shear fracture. In: Tillerson JR, Wawersik WR (eds) Paper presented at the 33rd US rock mechanics symposium, 908-816. Balkema, Rotterdam, pp 807–816
Mandl G (2005) Rock joints. The mechanical genesis. Springer, Berlin
Marschall P, Horseman S, Gimmi T (2005) Characterisation of gas transport properties of the opalinus clay, a potential host rock formation for radioactive waste disposal, oil & gas science and technology—rev. IFP 60(1):121–139
Martin CD (1997) Seventeenth Canadian geotechnical colloquium: the effects of cohesion loss and stress path on brittle rock strength. Can Geotech J 34:698–725
Martin CD, Chandler NA (1994) The progressive fracture of Lac du Bonnet granite. Int J Rock Mech Min Sci 31:643–659
Martin CD, Lanyon GW, Bossart P, Blümling P (2004) Excavation disturbed zone (edz) in clay shale: Mont Terri, Mont Terri Technical Report 2001-01
Millard A, Maβmann J, Rejeb A, Uehara S (2009) Study of the initiation and propagation of excavation damage zones around openings in argillaceous rock. Environ Geol 57:1325–1335
Mogi K (1962) Study of elastic shocks caused by the fracture of heterogeneous materials and its relations to earthquake phenomena. Bull Earthq Res Inst 40:125–173
Nagra (2002) Projekt Opalinuston—Synthese der geowissenschaftlichen Untersuchungsergebnisse. Technical Report of the National Cooperative for the Disposal of Radioactive Waste, NTB 02-03
Naumann M, Hunsche U, Schulze O (2007) Experimental investigations on anisotropy in dilatancy, failure and creep of Opalinus Clay. Phys Chem Earth 32:889–895
Niandou H, Shao JF, Henry JP, Fourmaintraux D (1997) Laboratory investigation of the mechanical behavior of tournemire shale. Int J Rock Mech Min Sci 34(1):3–16

Popp T, Salzer K (2007) Anisotropy of seismic and mechanical properties of Oplainus clay during triaxial deformation in a multi-anvil apparatus. Phys Chem Earth 32:879–888

Price NJ (1966) Fault and joint development in brittle and semi-brittle rock, Pergamon, New York

Rejeb A, Cabrera J (2006) Time-dependent evolution of the excavation damaged zone in the argillaceous Tournemire site. In: Paper presented at the GeoProc international conference on coupled T–H–M–C processes in geosystems, 22–25 May, Nanjing, P R. China, pp 65–74

Scholz CH (1968a) Microfracturing and inelastic deformation of rock in compression. J Geophys Res 73(4):1417–1432

Scholz CH (1968b) Experimental study of the fracturing process in brittle rock. J Geophys Res 73(4):1447–1454

Shah KR, Labuz JF (1995) Damage mechanism in stressed rock from acoustic emission. J Geophys Res 100(B8):15527–15539

Stefanizzi S, Barla G, Kaiser PK, Grasselli G (2008) Numerical modeling of rock mechanics tests in layered media using finite/discrete element approach. In: 12th international congress of IACMAG, Goa, India, pp 1126–1131

Tang CA, Liang ZZ, Zhang YB, Chang X, Tao X, Wang DG, Zhang JX, Liu JS, Zhu WC, Elsworth D (2008) Fracture spacing in layered materials: a new explanation based on two-dimensional failure process modeling. Am J Sci 3008:49–72

Tapponier P, Brace WF (1976) Development of stress-induced microcracks in Westerly Granit. Int J Rock Mech Min Sci 13:103–112

Thoeny R, Amann F, Button EA (2010) Ground conditions and the relationship to ground behavior—a new mine-by project in Opalinus clay at Mont Terri Rock Laboratory. In: Zhao J, Labiouse V, Dudt J-P, Mathier J-F (eds) Rock mechanics and environmental engineering. Paper presented at European Rock Mechanics Symposium 2010, Lausanne, Switzerland. Taylor & Francis Group, London, pp 775–778. ISBN 978-0-415-58654-2

Thury M, Bossart P (1999) Mont Terri Rock Laboratory, Results of the Hydrogeological, Geochemical and Geotechnical Experiments performed in 1996 and 1997, Landeshydrologie und -geologie, Geologischer Bericht Nr. 23

Underwood LB (1967) Classification and identification of shales. J Soil Mech Found Div Proc Am Soc Civ Eng 93:97–116

Valès F, Minh DN, Gharbi H, Rejeb A (2004) Experimental study of the influence of the degree of saturation on physical and mechanical properties in Tournemire shale (France). Appl Clay Sci 26:197–207

Van Loon LR, Soler JM, Müller W, Bradbury MH (2004) Anisotropic diffusion in layered argillaceous rocks: a case study with opalinus clay. Environ Sci Technol 38:5721–5728

Walsh JB, Brace WF (1966) Elasticity of rock; a review of some recent theoretical studies. Int J Rock Mech Min Sci 4:283–287

Yong S (2007) A three-dimensional analysis of excavation-induced perturbations in the opalinus clay at the Mont Terri Rock Laboratory. Ph.D-Thesis, Geological Institute, ETH Zurich (Diss. ETH No. 17575)

Yong S, Kaiser PK, Loew S (2010) The influence of pre-existing shears on tunnel-induced fracturing. Int J Rock Mech Min Sci 47:894–907

Zang A, Wagner ChF, Dresen G (1996) Acoustic emission, microstructure, and damage model of dry and wet sandstone stressed to failure. J Geophys Res 101(B8):17507–17521